LUND UNIVERSITY

LTH FACULTY OF ENGINEERING

A Refined Approach to Ultrafast Videography of Laser Filaments

Olivia Persson

Master's Thesis in Engineering Physics

Supervisor: Ass. Prof. Elias Kristensson

Co-supervisor: Dr. Vassily Kornienko

June 2026

Department of Physics,
Faculty of Engineering,
Lund University

A Refined Approach for Ultrafast Videography of Laser Filaments

Olivia Persson

LUND UNIVERSITY

LTH
FACULTY OF ENGINEERING

Thesis for Master of Science in Engineering Physics

Supervisor:	Ass. Prof. Elias Kristensson
Co-supervisor:	Dr. Vassily Kornienko
Examiner:	Prof. Mattias Richter

Department of Physics
Faculty of Engineering, Lund University

Abstract

This study presents the development and validation of a new, compact architecture for ultrafast videography using the Frequency Recognition Algorithm for Multiple Exposure (FRAME). Traditional FRAME-systems often have high mechanical complexity, long optical path lengths, and are limited to one-dimensional (1D) informational extraction of refractive index gradients when using Schlieren imaging. The proposed design solves these problems by using a common-path configuration that is based on a single Diffractive Optical Element (DOE), a lens, and simple delay plates of glass. This results in a reduced amount of optics and path length through glass to nearly a third of the previous setup. The experimental results show that a 1 mm thick glass plate generates a stable time delay of 1.7 ps for a 28 fs laser pulse, giving a frame rate of 0.6 THz. Theoretical calculations show a maximum frame rate of 30 THz when using thinner glass plates (down to $\sim$21 μm) before the pulses overlap in time. The scalability of the number of frames in the system is today limited by the DOE used rather than material dispersion. The critical limit, at which the pulses are broadened so much that they overlap, is at 400 mm of glass. Then, a method for three-beam interference is implemented to enable two-dimensional (2D) extraction of the refractive index gradient in a single exposure. The method is successfully validated through 2D Schlieren imaging of a flame from a Bunsen burner. In summary, the new architecture offers a stable, scalable, and robust setup for future recording of stochastic ultrafast phenomena such as the dynamic evolution of laser filaments.

Acknowledgment

First and foremost, I would like to thank my supervisors, Elias and Vasse, for their invaluable guidance and support through this project. Elias, your vibrant creativity and endless stream of ideas made everything feel possible and kept the project moving forward. Vasse, your constant availability and encouragement have been a huge support, guiding me reliably through both the breakthroughs and the setbacks of this work.

I am also deeply grateful to my friends and colleagues, both inside and outside the office. Thank you for all the shared laughter, the great discussions, and for always being there to talk through ideas or offer a helping hand. You made this journey so much more enjoyable.

Till min familj: Tack för er villkorslösa kärlek och ert stöd. Er nyfikenhet, ständiga uppmuntran och era perspektiv har varit till hjälp i alla mina beslut längs vägen.

Finally, a special thank you to Anton. Thank you for always being my rock and for standing firmly by my side through it all.

Contents

1 Introduction

Human perception of time is inherently limited and captures the world around us at a mere fraction of the speeds found in nature. In the timescales of picoseconds and femtoseconds, observing physical phenomena requires technology that exceeds biological limits, namely ultrafast optics. Such high temporal resolution is essential for understanding the complex interactions between high-intensity laser pulses and matter. This thesis focuses on the development of a compact and robust imaging architecture for visualizing the elusive dynamics of laser filamentation using a single-shot videography approach. This methodology pushes the boundaries of what can be captured in a single, rapid exposure which provides a window into events that have previously been too fast or too unpredictable to observe.

1.1 Background

A central phenomenon in non-linear optics is laser filamentation, which occurs when a high-intensity light pulse propagates through a transparent medium, such as air, creating a long plasma channel [1]. These filaments travel at speeds near the speed of light, approximately $3 \cdot 10^8$ m/s. Understanding the dynamics of this process is critical, yet challenging, as the interaction happens almost instantaneously and within media that provide low natural contrast.

The study of laser filamentation aims to understand its fundamental mechanics in order to better influence and utilize the process. Several applications have been proposed, most notably in LiDAR (Light Detecting and Ranging), where it is considered an excellent tool [2]. This technique performs remote measurements using light to reconstruct 3D images of objects and environments. LiDAR is used in fields such as atmospheric monitoring, topographic mapping, and archaeology. Laser filaments can extend for several kilometers and contribute a coherent white supercontinuum light emitted back toward the source, which absorption LiDAR can utilize as a light source for measurements [2, 3]. In atmospheric sensing, this opens up possibilities for multi-component analysis, increased precision, and measuring the size distribution of aerosols [3].

Laser filaments in air have also been shown to be useful for self-waveguiding to achieve highly directional amplified fluorescence [4]. This can increase the signal intensity by an estimated factor of 100, which is a major advantage for filament-based LiDAR [4]. Furthermore, there is hope to use laser filamentation for FIBS (Filament-Induced Breakdown Spectroscopy), a technique that analyzes emission spectra from atoms using the filament as an excitation source [2, 3]. Despite these potential applications, environmental challenges such as turbulence and low chemical concentrations persist, which complicates the sensing and imaging of multi-component pollutants [5].

Despite the potential of these applications, capturing the formation of a filament in real-time presents an immense technological challenge. Videography is a powerful tool for studying processes that are otherwise invisible to the naked eye. By manipulating frame rate, we can observe everything from slow geological changes to ultrafast atomic processes, where the greatest technological challenge lies in capturing phenomena that occur on extremely short timescales. Although modern sensor technology has evolved rapidly, conventional high-speed cameras are limited by an inherent electronic bottleneck during data readout [6]. The most specialized conventional sensors optimized for frame rates have shown speeds of 125 Mfps [6], and a theoretical upper limit of 90.1 Gfps [7]. For phenomena moving near the speed of light, such conventional sensors are insufficient. They fail to provide a short enough exposure time to eliminate motion blur, and the frame rate remains too low to track the rapid dynamics, leaving a 3.3 mm gap between consecutive frames.

With conventional high-speed cameras using a frame rate of 125 Mfps, the filament would travel 2.4 m between two exposures. This results in a video with significant motion blur, which makes it impossible to extract useful spatial information regarding the filament's structure. To enable the study of these events and their underlying phenomena, new videography methods are required that bypass these electronic limitations.

To overcome these constraints, researchers have developed alternative imaging strategies such as 'Pump-Probe' videography used to film events that can be replicated exactly multiple times [8]. It records sequentially by imaging the state of the process with increasing time delays [8], resulting in a video with both high temporal and spatial resolution. While this method can follow electron dynamics and was awarded the Nobel Prize [9], it is strictly limited to events that can be replicated exactly. Laser filaments, however, are inherently stochastic due to their structure changing with every laser shot, and sequential methods therefore fail to capture their true, non-repetitive dynamics.

This makes it necessary to use 'Snapshot' videography, which captures ultra-fast sequences in a single exposure. While techniques like Compressed Ultrafast Photography (CUP) exist, they often suffer from complex mathematical artifacts and reduced effective frame rates [10, 11]. In contrast, the Frequency Recognition Algorithm for Multiple Exposures (FRAME) utilizes spatial frequency modulation to provide a robust and direct reconstruction [12]. Furthermore, by integrating Schlieren imaging, a technique that converts refractive index gradients into visible intensity variations, into the FRAME architecture, it becomes possible to visualize refractive index changes in the transparent media where filaments propagate [13]. Consequently, FRAME stands out as a prime candidate for capturing the high-speed, stochastic, and transparent nature of laser filamentation.

1.2 Problem Statement

Despite the potential of FRAME, current setups have significant limitations. The existing architecture, as can be seen in Figure 1, is complex and requires a large number of optical components. This makes the system sensitive to external disturbances and results in an extensive need for time-consuming alignment. Furthermore, the large amount of glass that the laser pulses must pass through causes significant temporal dispersion [14]. This temporal broadening of the pulse directly degrades the system's temporal resolution. Finally, the current design is difficult to scale for capturing more sub-images, as the setup quickly becomes too bulky and the alignment too intricate.

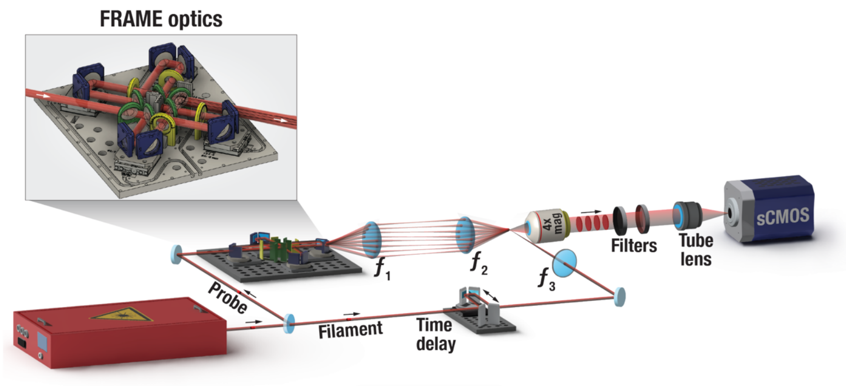

Figure 1: Schematics of a traditional FRAME setup [15]. This configuration requires several independent beam paths to create and modulate the individual sub-pulses, illustrating the high mechanical complexity and long optical path lengths of previous designs.

There are also limitations in the technique of combining Schlieren imaging with FRAME. Previous attempts have shown that the method works for capturing a single image of laser filaments. However, the information per image is limited by how much data can be encoded into each image.

To achieve high Schlieren resolution in two dimensions, two sequential images have traditionally been used. These two images store different information, which, when combined, provides high resolution. This works for slower objects, such as flames, which remain static on the timescale between the two images. However, it does not work for laser filaments, which change too rapidly, meaning the two sequential images no longer represent the same state. Consequently, only a single image has been feasible for laser filaments, resulting in lower Schlieren resolution. Currently, single-shot methods are largely restricted to capturing refractive index gradients in a single dimension [13]. To achieve full 2D gradients for laser filaments that match the resolution achievable in static or slow-moving phenomena like flames, all necessary information must be multiplexed into a single frame. This work investigates the use of interference between multiple beams to create advanced reference patterns, enabling the encoding of more complex spatial information within every sub-image.

Thus, there is a need to develop a more robust and compact FRAME design that minimizes the number of optics to maintain short pulse lengths, while simultaneously allowing for simplified scalability of the number of sub-images. A design is also needed that can handle complex reference patterns to enable measurements in two spatial dimensions, thereby maximizing the spatial information that can be extracted regarding the filament's structure in every single exposure.

1.3 Objectives and Research Questions

This thesis aims to design, implement, and validate a compact FRAME setup that improves temporal resolution and enables more comprehensive spatial information extraction. The work focuses on minimizing optical complexity and investigating new methods for generating reference patterns for single-shot 2D Schlieren videography.

To achieve this, the following objectives are defined:

- **Objective 1:** Develop a robust FRAME setup with a minimized number of optical components to limit temporal dispersion and simplify experimental alignment.
- **Objective 2:** Develop an architecture that allows for easy scaling of the number of sub-images to increase the system's total sequence length.
- **Objective 3:** Implement a method for generating complex reference patterns (via three-beam interference) to enable the extraction of refractive index gradients in two dimensions.
- **Objective 4:** Validate the system's 2D Schlieren capability by imaging the refractive index gradients of a Bunsen burner flame.

Based on these objectives, the study aims to answer the following research questions:

1. How much can the total material path length (glass thickness) be reduced in the new design compared to previous FRAME setups, and what is the calculated effect on the laser pulse duration?
2. In what way does the new compact design facilitate the scaling of the number of sub-images in the sequence, and what are the design limitations for the system's maximum sequence length?
3. Is it possible to experimentally generate a stable pattern via three-beam interference, and how does this affect the ability to extract 2D Schlieren information in a single exposure?

1.4 Scope and Limitations

This project focuses on the design and experimental verification of a new FRAME setup. To generate reference patterns, the study specifically investigates three-beam interference created using a diffractive optical element (DOE) and a focusing lens. The goal of the work is to demonstrate the technique as a proof-of-concept.

Existing software will be used for the reconstruction of images from FRAME and Schlieren data; the development of new reconstruction algorithms is therefore outside the scope of this work. Furthermore, the emphasis is on instrumental development, meaning that no extensive analysis of the underlying physics of laser filaments will be performed. In this context, the phenomenon serves primarily as a test object to evaluate the performance of the videography method. The project is conducted within the framework of a 30 ECTS Master's thesis, which sets a natural time limit for system optimization and the number of experimental measurement series.

2 Theoretical Background

This chapter presents the theoretical foundations underpinning this work. First, the principles of the Frequency Recognition Algorithm for Multiple Exposures (FRAME), a method for encoding temporal information into spatial frequencies, are described. This is followed by a discussion on the physics of ultrashort laser pulses and how dispersion affects the system's temporal resolution. Furthermore, the Schlieren methodology for visualizing refractive index gradients is introduced. Finally, the use of optical interference and diffractive elements to generate the necessary reference patterns is detailed. Throughout this chapter, the focus is placed on the physical trade-offs and limitations, such as spatial resolution versus crosstalk, dispersion versus material thickness, and 1D versus 2D phase sensitivity, that directly motivate the design choices and objectives of this thesis.

2.1 Principles of FRAME

Studying phenomena moving near the speed of light requires a shutter speed millions of times faster than what even the fastest conventional electronics at speeds of 125 Mfps [6] can achieve. A typical mechanical or electronic shutter in a modern CMOS camera has an exposure time ranging from microseconds (10^{-6} s) to milliseconds (10^{-3} s). However, physical processes occurring near the speed of light, such as laser filamentation, take place on much shorter timescales. To overcome the physical speed limits of standard electronic sensors, alternative optical gating techniques must be employed. This chapter begins with an overview of the FRAME method, which encodes time into spatial frequencies to achieve exceptionally fast effective shutter speeds, placing it firmly within the field of ultrafast videography.

2.1.1 Spatial Frequency Coding

With FRAME, a conventional camera is transformed into an ultrafast video camera by utilizing a pulse train of ultrashort laser pulses. This creates an ultrafast stroboscopic effect where the laser pulses, rather than the mechanical shutter, dictate the exposure time. The pulse train is created by dividing an original laser pulse into several sub-pulses, while maintaining the original pulse duration, and then separating the sub-pulses in time. Each pulse in the train illuminates the object at a unique point in time. If these pulses hit the camera sensor sequentially during a single exposure, the sensor records a superimposed image where the information from all individual pulses, and thus the temporal evolution of the event, is mixed and lost.

To distinguish the sub-images afterward, a unique signature is required for each pulse. This signature is created by modulating each sub-image with a unique spatial carrier wave in the form of an interference pattern with a known spatial frequency (see Figure2, where the pattern is identical but rotated by 20° between the first and second pulse). The concept is similar to radio technology, where different radio channels are transmitted simultaneously but separated by modulation onto different carrier frequencies. By varying the frequency or rotation of the reference pattern for each pulse in the train, the information from each point in time can later be identified in specific parts of the image spectrum and extracted. A strength of FRAME is that the method requires no prior knowledge of the object's appearance since it relies entirely on the knowledge of the chosen reference patterns and the temporal order in which they are introduced. However, as more pulses are introduced to increase the number of sub-images, the complexity of multiplexing these carrier frequencies increases, which is a challenge that directly underscores the need for scalable optical architectures.

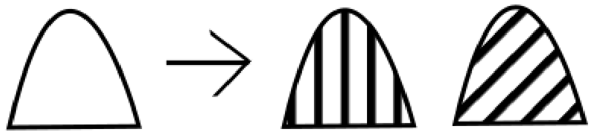

Figure 2: Conceptual overview of spatial frequency coding in FRAME. A single ultrashort laser pulse is split into a pulse train where each sub-pulse is separated in time. To uniquely tag the temporal information, each sub-pulse is modulated with a specific spatial carrier frequency.

2.1.2 The Fourier Plane and Image Separation

The separation of sub-images is made possible by analyzing the image in its frequency plane, also known as the Fourier plane. In optics, a convex lens can naturally perform a Fourier transform on an object placed in the lens's front focal plane, producing a spatial frequency spectrum in the rear focal plane [14].

In this optical Fourier plane, information is separated based on its physical structure. A sinusoidal striped pattern in the image plane (the spatial domain) corresponds to two distinct points (frequency components) in the Fourier plane. Experimentally, these necessary spatial frequencies are generated using optical elements such as diffraction gratings or diffractive optical elements (DOEs). By using multiple optical components of this kind, each with unique patterns, pairs of points are added to the physical Fourier plane. Low frequencies originating from large structures in the image and the background gather near the center of the plane (the optical axis), while high frequencies from fine details and periodic patterns are located further from the center. A point in this plane is defined by its distance from the center (magnitude), corresponding to the density of the pattern, and its angle, corresponding to the rotation of the pattern.

After the superimposed image is captured by the camera sensor, the separation and recovery of the sub-images are performed digitally. By applying a digital Fourier transform (FFT) to the recorded image, the spatial modulation introduced in the optical setup can be analyzed mathematically.

When the image of the object is multiplied by the reference pattern in the spatial domain, it can be mathematically modeled as a cosine wave, $1 + \cos(k_0 x)$, where k_0 denotes the spatial carrier frequency and x is the spatial coordinate. According to the convolution theorem, this multiplication corresponds to a convolution in the Fourier domain [14]. Since the Fourier transform of a cosine wave consists of two separate Dirac delta functions, the convolution shifts the object's spatial frequency spectrum by the carrier frequency $\pm k_0$ [14]. This shift is what mathematically generates the isolated frequency components in the digital Fourier plane, allowing each sub-image to be filtered out and recovered. This information, of sharing a mechanism within the finite space of the Fourier domain, implies that any physical addition of new sub-pulses must be highly optimized to limit crosstalk, establishing a fundamental boundary when scaling total sequence lengths.

2.1.3 Digital Image Reconstruction

The reconstruction of the video sequence is performed digitally through post-processing. By performing a Fast Fourier Transform (FFT) on the raw image, the user can identify the known frequency components for each sub-image. Applying a digital filter (masking) around a specific frequency component and then performing an Inverse Fourier Transform (IFFT) allows the sub-image for that specific point in time to be reconstructed without the reference pattern.

This process highlights the core trade-off of the FRAME method, that spatial resolution is sacrificed to gain temporal information. The spatial resolution of each reconstructed frame depends entirely on the size of the digital filter used to isolate the frequency information in the Fourier domain. As more sub-images are multiplexed onto the sensor, their corresponding signal clusters occupy a larger portion of the total Fourier plane. To prevent these adjacent filters from overlapping, the digital filters must be made smaller. If two filters overlap, spatial frequency crosstalk occurs, causing information from different points in time to leak into one another. Consequently, accommodating a longer pulse train forces a reduction in individual filter size. The spatial bandwidth is limited by how much of the Fourier plane can be allocated to each sub-image. When the size of the filters (masks) is reduced to avoid overlap between adjacent frequency components, the higher spatial frequencies of the image are filtered out. This results in reduced spatial resolution and unavoidable blurring in the reconstructed image. If, on the other hand, the masks are made too large, crosstalk occurs, where information from one sub-image leaks into another, creating artifacts. The optimal mask size is thus a balance between maximizing spatial resolution and minimizing crosstalk.

After the spatial frequency components have been isolated and the inverse Fourier transforms completed, a time-resolved sequence of individual sub-images is obtained. By knowing the exact temporal sequence of the applied reference patterns, these sub-images can be arranged chronologically. In this way, the static, superimposed image is assembled into a video sequence with a frame rate dictated by the temporal spacing between the laser pulses.

2.2 Ultrafast Laser Pulses and Dispersion

As described in the previous section, the laser pulse acts as the system's shutter. A fundamental requirement for FRAME is therefore that these pulses remain extremely short in time to maintain a high temporal resolution and avoid motion blur. However, when femtosecond pulses propagate through the optical elements required by the setup—such as lenses, DOEs, and beam splitters - they inevitably interact with the material.

This interaction leads to dispersion, a phenomenon where the different frequency components of the pulse travel at different speeds, causing the pulse to stretch temporally. Analyzing this degradation is vital, as evaluating the reduction of total material path length (glass thickness) and its direct numerical effect on pulse duration forms a core investigative question of this study. To understand how this limits the performance of FRAME, it is essential to first analyze how these ultrafast pulses are characterized, how dispersion arises physically, and how it mathematically scales with the pulse properties and the amount of glass in the system.

2.2.1 Characterization of Femtosecond Pulses

An ultrafast laser pulse is characterized by its temporal width, often measured in femtoseconds (10^{-15} s). To visualize this timescale, light travels approximately 0.3 μm in one femtosecond. According to the uncertainty principle, there is a fundamental relationship between the pulse's temporal width (Δt) and its spectral width ($\Delta \nu$):

$$\Delta t \cdot \Delta \nu \geq C \tag{1}$$

where C is a constant depending on the pulse shape (e.g., 0.431 for a Gaussian pulse) [14]. This means that the shorter a pulse is in time, the broader its spectrum (bandwidth) must be. A femtosecond pulse thus consists of many different wavelengths that interact through constructive interference to form the short pulse. Figure 3 illustrates this concept, showing how several continuous cosine waves of different frequencies interfere constructively at a specific point in time to form a localized pulse, while interfering destructively elsewhere.

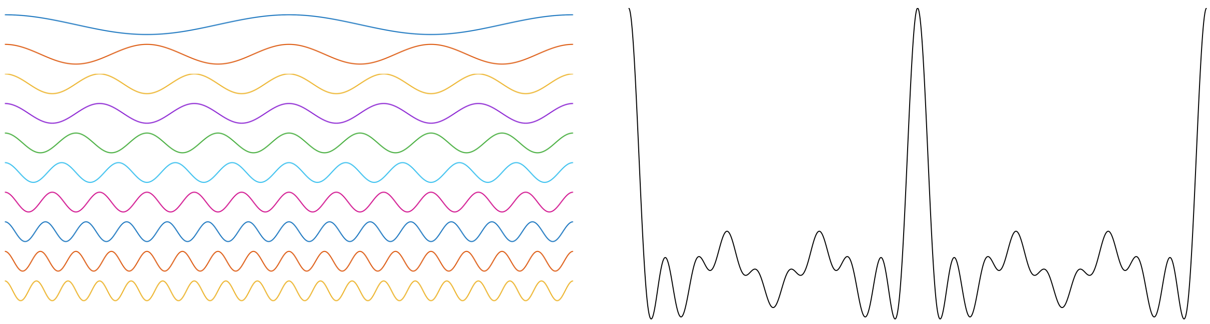

(a) A spectrum of continuous cosine waves with varying frequencies propagating in phase.

(b) The mathematical superposition of the cosinus waves, resulting in a highly localized temporal pulse.

Figure 3: Conceptual formation of an ultrashort laser pulse. The continuous cosine waves overlap in phase, leading to strong constructive interference at a single point in time, while destructive interference dampens the amplitude elsewhere.

When such a pulse propagates through different media, its travel time is altered due to changes in the refractive index. The temporal delay ($\Delta\tau$) that a pulse experiences when traveling a distance z through glass compared to air can be expressed as [14]:

$$\Delta\tau = \frac{z}{c}(n_{\text{glass}} - n_{\text{air}}) \tag{2}$$

For a glass thickness of $z = 1$ mm, and assuming $n_{\text{glass}} \approx 1.5$ and $n_{\text{air}} \approx 1.0$ [14], this delay becomes approximately 1.67 picoseconds.

2.2.2 Group velocity Dispersion (GVD)

When a light pulse travels through a medium such as glass (e.g., fused silica), it slows down compared to vacuum. This is described by the refractive index, defined as:

$$n(\nu) = \frac{c_0}{c(\nu)} \tag{3}$$

where n is the refractive index, c is the velocity in the medium, and c_0 is the speed of light in vacuum [14]. The speed of light in a medium, and thus the refractive index, is frequency-dependent (ν), a phenomenon known as dispersion. In most optical glasses, normal dispersion occurs, meaning that higher frequencies (blue light) experience a higher refractive index and thus travel more slowly than lower frequencies (red light) [14]. This leads to the pulse becoming "chirped," meaning its different color components are separated in time, and the pulse is stretched in time [14]. To understand this mathematically, one considers the pulse's shape, its so-called envelope. It is the envelope that carries energy and information [14] and thus acts as the shutter for sub-images when using FRAME. The individual oscillations within the pulse travel at the phase velocity, and the difference between the phase velocities of the various wavelengths that build the pulse causes it to deform. The speed at which this envelope moves is called the group velocity (v_g). In a dispersive medium, different frequency components experience different amounts of delay, causing the envelope to deform. This effect is called Group Velocity Dispersion (GVD), and its impact on the pulse width increases with the amount of glass [14].

2.2.3 Temporal Pulse Broadening and FRAME

In FRAME, the temporal width of the laser pulse limits the system's exposure time. If the pulse is stretched due to dispersion in lenses and beam splitters, the risk of motion blur increases. For a phenomenon moving at the speed of light, such as a laser filament, an increase in pulse width from, for example, 100 fs to 200 fs means the object moves an additional 30 μm during exposure. Since motion blur represents a permanent loss of spatial information that cannot be digitally restored, it is critical to minimize the amount of glass in the system to maintain a shutter speed that is adequate for the event under observation. The temporal broadening of a pulse (σ_τ) after propagating a distance z through a dispersive medium depends on the spectral width (σ_ν) and the group velocity dispersion (GVD) parameter (D_ν). This relationship, along with the definitions of GVD and group velocity (v_g) in terms of the frequency-dependent refractive index $n(\nu)$ and the speed of light in vacuum (c_0), can be expressed as [14]:

$$\sigma_\tau = |D_\nu|\sigma_\nu z \tag{4}$$

$$D_\nu = \frac{1}{d\nu}\left(\frac{1}{v_g}\right) \tag{5}$$

$$\frac{1}{v_g} = \frac{1}{d\nu}\left(\frac{\nu n(\nu)}{c_0}\right) \tag{6}$$

By differentiating the inverse group velocity with respect to frequency, the total temporal broadening can be combined into a single expression:

$$\sigma_\tau = \frac{1}{d\nu^2}\left(\frac{\nu n(\nu)}{c_0}\right)\sigma_\nu z \tag{7}$$

Equation (7) shows that shorter pulses are more sensitive to broadening than longer pulses, as a shorter pulse duration corresponds to a broader spectrum (larger σ_ν). In FRAME, managing this trade-off is critical because motion blur acts as a permanent loss of information. When an object moves while the shutter is open, details are spread across multiple pixels; there is no mathematical method that can reconstruct this lost information afterward. This physical constraint establishes a strict design requirement for the imaging system, necessitating a highly compact optical configuration with a minimized component count to suppress pulse stretching at its physical source.

2.3 Schlieren Imaging

Once the technique for capturing ultrafast images is established, a method is required to visualize the objects under study. This work focuses on phenomena such as laser filaments, which induce rapid, transient changes in the refractive index of air.

To effectively capture these phase objects (i.e., transparent objects that alter the phase of light rather than its intensity, such as flames or gas flows), the region where the filamentation occurs must be precisely aligned with the object plane of the Schlieren imaging system. When an imaging system is focused exactly on this object plane, any spatial phase variations or light deflections caused by the filament are mapped onto corresponding intensity variations at the camera sensor. If the object deviates from the object plane, the spatial carrier pattern itself remains in focus, but the spatial distribution of the deflected light is distorted. This displacement reduces the geometric resolution of the phase features and introduces blurring to the reconstructed structures. The physical mechanisms causing these refractive index variations and how they affect the probe light are detailed below.

2.3.1 Refractive Index Gradients

The refractive index (n) describes the ratio between the speed of light in a vacuum (c_0) and its velocity within a medium (c), serving as a fundamental measure of how much the light slows down. In a gaseous medium like air, this index is not static. It changes primarily due to local density variations caused by phenomena such as thermal fluctuations, shockwaves, or plasma formation [14].

In the context of this work, the formation of laser filaments is of primary interest. When an ultrashort and intense laser pulse propagates through air, it induces an intensity-dependent refractive index via the optical Kerr effect. This phenomenon is described by [14]:

$$n(I) = n_0 + n_2 I \tag{8}$$

where n_0 is the medium's linear refractive index, n_2 is the nonlinear refractive index coefficient, and I is the local intensity of the laser. Since the laser beam's intensity profile is highest at its center, the medium temporarily acts as a positive lens, causing the beam to self-focus [14]. As the beam self-focuses, its spatial intensity increases drastically until it reaches a critical threshold where the photon energy becomes high enough to ionize the surrounding gas molecules, creating a plasma. The free electrons in this newly formed plasma contribute to a local decrease in the refractive index, which results in a strong defocusing effect [1]. Laser filamentation is the result of this dynamic balance between Kerr-induced self-focusing and plasma-induced defocusing, allowing the pulse to propagate over long distances without diverging.

This dynamic process creates strong spatial refractive index gradients (∇n) in the air. When an external probe light (e.g., from an LED or a secondary laser) crosses this filament region perpendicularly, it encounters these inhomogeneous gradients. According to the general form of Snell's law for inhomogeneous media, light rays traversing such a region are continuously bent toward areas with a higher refractive index [14]. The resulting total deflection of the probe light is proportional to both the strength of the gradient (∇n) and the path length through the filament. It is precisely this microscopic deflection of light rays that Schlieren imaging is designed to capture and visualize.

2.3.2 From Deflection to Intensity Variations

In conventional Schlieren imaging, parts of the deflected light are blocked with a knife-edge, converting deflection changes into intensity variations. In FRAME-Schlieren, the encoded reference pattern is used instead. When light is bent by an object, the reference pattern is locally deformed, and this deformation is captured by the sensor. By comparing the deformed pattern with a reference image taken without the object, the software can calculate how much the light has been deflected. This workflow is shown in Figure 4, where the deflection of light due to the heat of a candle is visualized using Schlieren imaging.

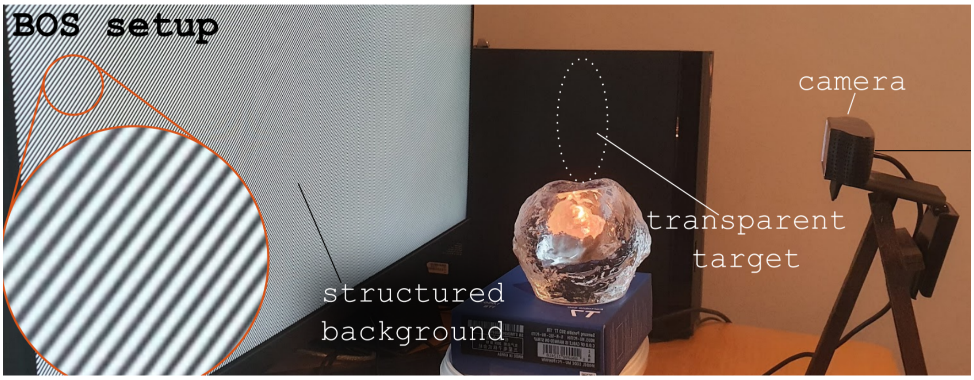

(a) Experimental imaging setup where a camera records the heat rising from a candle flame against a background grid of straight lines.

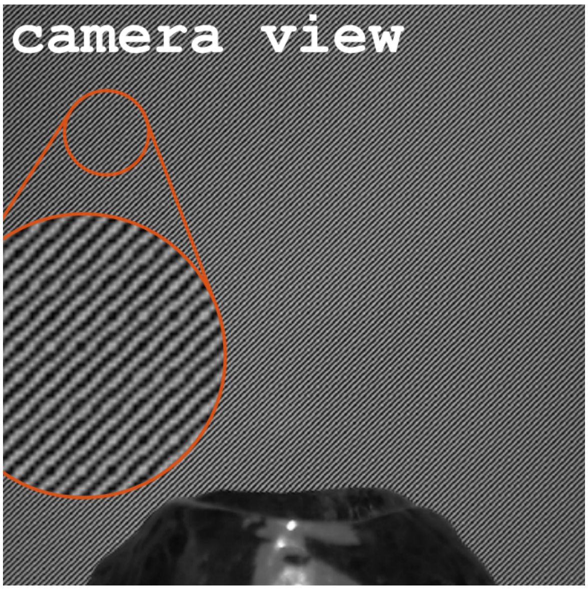

(b) The raw image captured by the camera, showing how the hot air bends the light and causes the background lines to become wavy and deformed.

(c) The final gradient map generated by the software, visualizing the physical deflection of light caused by the heat from the candle.

Figure 4: Conceptual workflow of pattern-based Schlieren imaging, demonstrating how background fringe deformations are utilized to reconstruct light deflection maps. Adapted from [13].

However, using a simple one-dimensional fringe pattern means that only the component of the refractive index gradient ∇n perpendicular to the fringes can be detected. To obtain a complete description of the refractive index gradient as a vector field in 2D, which is required for a complex object like a laser filament, a reference pattern with carrier waves covering multiple directions simultaneously is necessary. This limitation directly motivates the use of three-beam interference to generate a two-dimensional modulation pattern. Consequently, expanding the measurement capability to capture omnidirectional deflections requires a shift toward more advanced optical architectures capable of multi-directional carrier modulation. It is important to distinguish between the system's spatial resolution (the ability to reproduce small details in the object) and its phase sensitivity (the ability to detect small refractive index gradients). While spatial resolution is limited by the mask size in the Fourier plane, phase sensitivity is determined by the contrast and spatial frequency of the reference pattern.

2.4 Optical Interference and Pattern Generation

The final step is the practical creation of the 2D pattern required for both FRAME and Schlieren in a single optical setup, thus allowing for ultrafast videography of refractive index gradients such as filamentation. For the Schlieren method to detect complex refractive index gradients, a structured reference pattern is necessary. Traditional fringe patterns limit measurements to one dimension. To enable full 2D detection, more advanced pattern generation is required, which in this system is realized through optical interference between three beams. This pattern serves both as the spatial carrier wave for FRAME encoding and as the reference grid for the Schlieren measurement. By utilizing a unified optical assembly to simultaneously address the needs of both subsystems, the layout remains structurally optimized, establishing a versatile platform suitable for the practical evaluation of real-world refractive index gradients.

2.4.1 Two-Beam and Three-Beam Interference

Interference between two plane waves at an angle θ creates a sinusoidal fringe pattern. The periodicity d is given by [14]:

$$d = \frac{\lambda}{2 \cdot \sin(\frac{\theta}{2})} \tag{9}$$

By instead allowing three beams to interfere, a hexagonal grid pattern is created. As illustrated in Figure 5, this complex 2D structure is a direct result of superimposing three individual two-beam fringe patterns at different relative angles. It physically provides three pairs of points in the Fourier plane. This 2D grid is optimal for Schlieren imaging as it enables the detection of light deflection in all directions within the image plane.

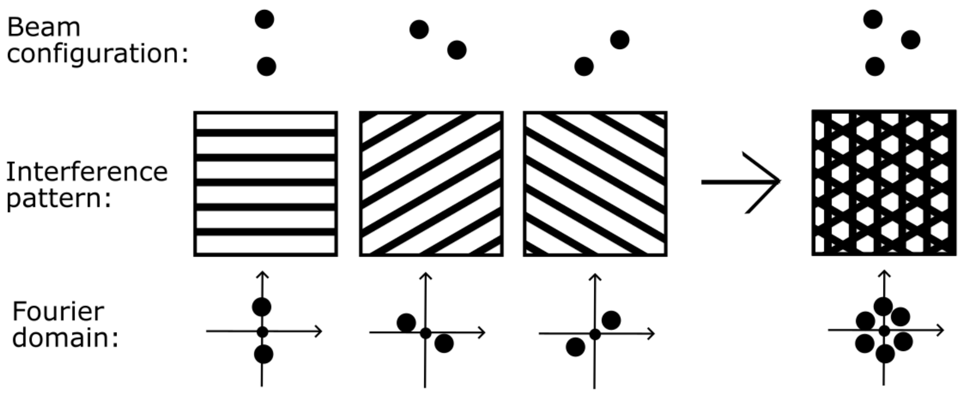

Figure 5: Schematic breakdown of pattern generation through optical interference, illustrating the relationship between the beam configuration (top row), the resulting spatial interference pattern (middle row), and its mapping in the Fourier domain (bottom row). The first three columns demonstrate how individual pairs of two beams form one-dimensional fringe patterns and corresponding conjugate spot pairs. The final column shows how the simultaneous superposition of all three beams forms the composite two-dimensional hexagonal grid, generating the three pairs of frequency components used for spatial carrier coding.

To mathematically describe the formation of this hexagonal grid, the total intensity distribution can be derived by considering the interference of three coherent plane waves. The resulting intensity pattern $I(\mathbf{r})$ from three interfering plane waves can be described by the superposition principle for the beams' electric fields E_n as [14]:

$$I(\mathbf{r}) \propto |\sum_{n=1}^{3} E_n e^{i\mathbf{k}_n \cdot \mathbf{r}}|^2 \tag{10}$$

where $\mathbf{k}_n$ is the wave vector for the n-th beam and $\mathbf{r}$ is the position vector in the observation plane. Expanding this squared sum yields cross-terms of the form $e^{i(\mathbf{k}_n - \mathbf{k}_m)\cdot\mathbf{r}}$. Physically, this expansion corresponds to breaking the three-beam system into three distinct pairs, as illustrated in the first three columns of Figure 5. Each pair acts as a spatial carrier wave with a frequency dictated by the difference vector $\Delta\mathbf{k} = \mathbf{k}_n - \mathbf{k}_m$. Because a single pair generates two conjugate spots, the full combination of the three beams yields the six characteristic points shown in the final column's Fourier domain.

The orientation of the incoming beams determines the direction of the pattern. For instance, when two beams are aligned vertically, as shown in the first column of Figure 5, the resulting fringe pattern is horizontal, translating to a vertical pair of conjugate spots along the axis in the Fourier domain. For the complete three-beam configuration, six frequency components arise in the Fourier domain, as each unique pair of the three beams contributes two symmetric points. It is also possible to interfere with more than three beams, which does not increase dimensional resolution but can improve the contrast between the pattern's peaks and troughs, enhancing measurement sensitivity.

2.4.2 Diffractive Optical Elements (DOE)

To generate these three beams with high precision and minimal dispersion, a Diffractive Optical Element (DOE) is used. A DOE is a specially designed glass element that splits an incoming beam into multiple beams at precise angles through diffraction. Using a DOE is advantageous over traditional beam splitters as it replaces several bulky components with a single thin element, minimizing the amount of glass and thus the dispersion in the system. Consequently, the integration of a single diffractive element serves as a key design mechanism, enabling a highly compact optical layout that minimizes material dispersion to preserve pulse duration, while simultaneously establishing a scalable pathway for expanding the temporal sequence length.

3 Experimental Methodology

This section details the experimental design, optical configurations, and laboratory procedures implemented to fulfill the goals of this study. The methodology is structured into three main parts: the physical experimental setup, the specific experimental procedures conducted in the laboratory, and the subsequent data analysis and image reconstruction workflow.

3.1 Experimental Setup and Optical Architecture

An experimental setup was constructed to transform a laser pulse into a pulse train in a compact, controlled, and robust manner, where each pulse carries its own unique reference pattern. This unique spatial frequency encoding ensures that multiple temporal frames can be simultaneously recorded on a single sensor exposure and subsequently isolated in the Fourier domain. The setup is illustrated in Figure 6, where a custom-designed Diffractive Optical Element (DOE) serves as the primary multi-beam generator. The DOE is a silicon wafer component with manufactured nanostructures, optimized for a specific wavelength. By utilizing a single lens that makes it possible to manipulate these beams in the spatial frequency domain, the architecture eliminates the multi-line component layout characteristic of traditional FRAME systems. To create the pulse train, the initial laser pulse is divided into several beams, which are then delayed in time relative to one another. The interference pattern for each pulse in the train is generated through multi-beam interference. For instance, if the original pulse is split into six beams and three of these are delayed, a pulse train consisting of two pulses is formed, where each pulse is characterized by a pattern from three interfering beams.

The pattern resulting from the interference of three beams provides the potential for higher resolution of refractive index gradients when measuring phenomena such as laser filaments. Similar refractive index variations occur in flames, albeit on a much slower timescale. Therefore, a continuous-wave (CW) laser was used with the same setup, but employing only a single pattern, to investigate the refractive index gradient resolution provided by three-beam interference when illuminating a flame from a Bunsen burner.

3.1.1 Optical Layout and Component Selection

The optical architecture (Figure 6) is designed to minimize the total amount of glass in the system, a critical factor for limiting pulse broadening due to dispersion. The system is based on a configuration where a Diffractive Optical Element (DOE) is placed before a single convex lens ($f = 300$ mm). Unlike traditional setups that require multiple beam splitters and long optical paths to create a pulse train, the DOE here generates all sub-beams simultaneously. The convex lens focuses these diffracted beams toward its rear focal plane, which naturally acts as the spatial Fourier domain. In this plane, the spatial frequencies of the beams are physically separated into a static grid of focal spots, as illustrated in Figure 7. This spatial separation allows for direct manipulation of the optical signal, where a custom spatial mask can block unwanted diffraction orders, and thin glass elements can be selectively inserted into specific beam paths to introduce localized optical delays.

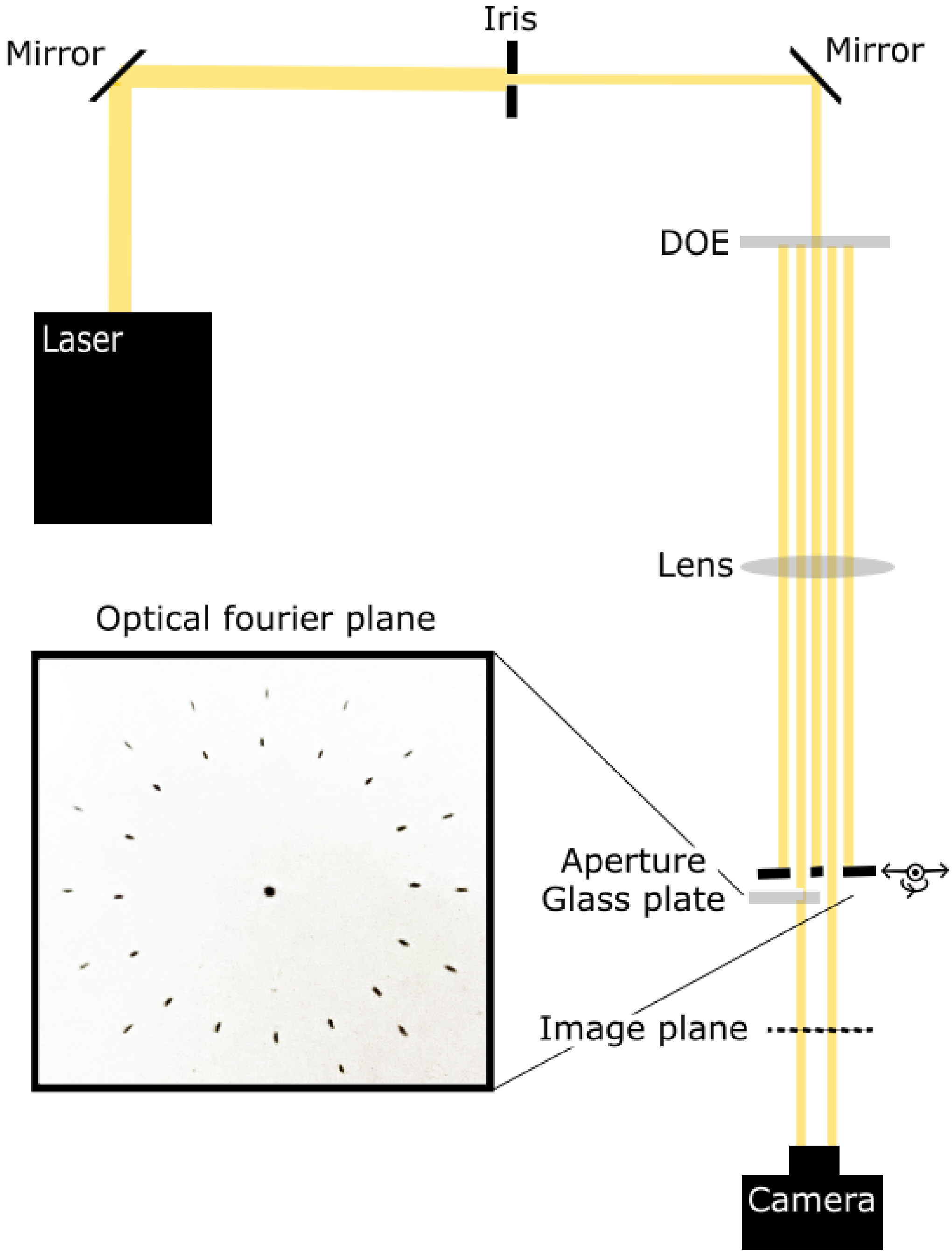

Figure 6: Schematic layout of the compact FRAME architecture. An initial laser pulse is split into a multi-beam matrix by the DOE, which is positioned prior to a single convex lens (f = 300 mm). The rear focal plane of the lens acts as the optical Fourier plane (showing a real image of the beam pattern), allowing for spatial selection via a custom aperture mask adjustable in translation and rotation (indicated by the directional arrows). The sub-beams are then overlapped at the object plane to create the spatial carrier patterns.

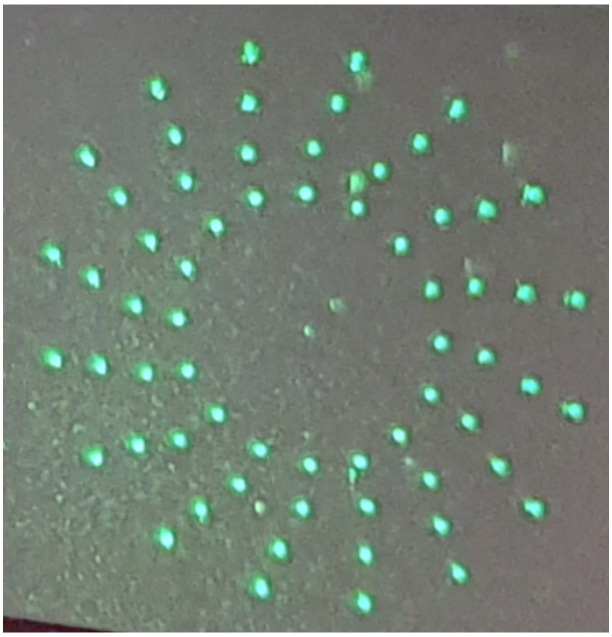

Figure 7: Photograph of the 64-beam matrix generated in the Fourier plane by the custom DOE. Adapted from [15].

The proposed architecture allows for a significantly more compact design compared to previous configurations (see Figure 1). By using a DOE to generate all sub-beams simultaneously, the need for multiple beam splitters and long optical delay lines is reduced. The static dimensions of the system, the distance from the DOE to the image plane, are determined by the focal length of the lens, which dictates the spacing between the DOE and the lens, as well as between the lens and the aperture. While any convex lens focal length can be chosen, this choice affects the spatial separation of the beams in the focal plane. A larger focal length provides a less dense focus, offering more room for physically manipulating the adjustable aperture stage and the glass plates used for temporal delays. A detailed breakdown of how these individual components modulate the beam spacing and timing is provided in the subsequent sections. In this setup, two mirrors and an iris were used to guide the light, with the iris acting as a spatial mask to clip the edges of the Gaussian beam.

When a laser pulse passes through glass, it is affected by dispersion and broadens in time, as described in Section 2.2. The components contributing to dispersion in this setup include the DOE, the lens, and the glass plates used for temporal delay. The total glass path is approximately 11 mm (DOE and lens $\sim$ 5 mm each, and the delay plate $\sim$ 1 mm). This glass thickness has been minimized to reduce Group Delay Dispersion (GDD), as described in Section 2.2.2, thereby maintaining high temporal resolution. The laser pulses have a duration of $\sim$ 28 fs, and the time delay between a beam passing through 1 mm of glass versus air is $\sim$ 1.7 ps. This deliberate glass-induced delay is the core mechanism used to synthesize a discrete pulse train from a single initial pulse, effectively converting an ultrafast event into a high-speed sequential video sequence.

The parameters used for the setup include a lens with a focal length of 300 mm, an ANDOR DL-604M-OEM camera for the pulsed laser (to demonstrate the new FRAME architecture), and an ANDOR ZYLA-5.5-USB camera for the CW laser (to demonstrate the Schlieren method). A custom spatial filter mask was also used, consisting of stiff paper with manually punched holes, mounted on a stage with degrees of freedom in translation (vertical and lateral) and rotation, as illustrated by the adjustment arrows in Figure 6.

3.1.2 Laser Sources and Beam Splitting

Two laser sources were used for the experiments: a pulsed femtosecond laser with a wavelength of 840 nm and a continuous-wave (CW) laser at 532 nm (THORLABS CPS532). The pulsed laser was used to generate pulse trains from a single pulse to verify the FRAME architecture.

The DOE used is optimized for 532 nm, while the pulsed laser operated at 840 nm. Consequently, the DOE does not split the incoming beam with maximum efficiency, resulting in a "zero-order" beam that passes through the center along the original optical axis.

3.1.3 Beam Realignment and Pulse Train Configuration

The DOE splits the incoming laser beam into several parallel beams in a pattern shown in Figure 7. While standard commercial DOEs often split a beam into two, this custom-ordered DOE splits the light into 64 beams. Since not all beams were necessary for these experiments, the beams of interest had to be manually selected while blocking the rest. To achieve this, an aperture was designed for the specific pattern and its dimensions (determined by the lens focal length). The aperture was created by placing thermal paper in the beam path to mark the positions of the spots. These marks were then used to punch holes in stiff paper for the desired beams, allowing them to pass while the remaining beams were blocked. Once the aperture was created, it required alignment to match the beams. A mounting stage with three degrees of freedom (horizontal and vertical translation perpendicular to the optical axis, and rotation) was constructed to facilitate this alignment.

The delay between pulses was created using a 1 mm thick glass plate. This plate was placed in the path of the specific beams intended for temporal delay after they had been selected by the aperture. For example, if two sets of three beams are selected and one set is delayed, a pulse train consisting of two pulses is formed. The temporal spacing between these pulses can be directly adjusted by varying the thickness of the glass plate according to Equation 2.

To experimentally demonstrate the scalability of this architecture, the setup was also configured to generate a three-pulse train. This extension was achieved by deploying two stacked 1 mm thick glass delay plates in the optical Fourier plane instead of just one. In this configuration, the selected beams are divided into three groups of pairs: the first pair propagates unhindered through air to form the leading pulse, the second pair passes through a single glass plate to introduce the first delay step, and the final pair traverses both glass plates sequentially to receive a double delay.

The choice of beams directly influences the interference pattern based on their mutual distance and angles. A larger distance between the beams results in a denser (higher frequency) pattern according to Equation (9). Since the camera has a limit on the spatial frequency it can resolve, the beam spacing was adjusted to optimize the pattern frequency while remaining within the sensor's resolution limits.

The layout of the spatial mask was designed so that the selected three-beam groups (trios) share identical, congruent geometries. This geometric symmetry ensures that each sub-image is encoded with a consistent spatial reference pattern, varying only by a controlled rotation on the sensor. Furthermore, this grouped arrangement simplifies the temporal delay stage. Because each beam trio corresponds to a single, discrete time step, the 1 mm glass delay plate can be positioned to uniformly retard one entire trio at once without intersecting the paths of the other beams. Based on these criteria, the final optical configuration was aligned as illustrated in Figure 8.

Figure 8: The spatial filter mask configured in the Fourier plane to select two independent triads of beams (six beams total) while blocking the remaining diffraction orders.

Because the laser pulses are only a few dozen femtoseconds long, the window for overlapping the pulses from the three beams in a trio is extremely narrow. However, the optics are inherently designed such that each beam arrives at the object plane simultaneously, meaning the three beams forming a pulse arrive in synchronization without requiring additional adjustment.

The resulting interference pattern in the image plane depends on the geometric relationship between the three beams. This can be understood as three pairs of beams, each forming a fringe pattern perpendicular to the line connecting them. If the beams are arranged symmetrically in an equilateral triangle, the pattern becomes a symmetric hexagonal or triangular grid, as seen in Figure 5. Different beam arrangements produce similar patterns but with varying spatial characteristics. The overall rotation of the pattern is determined by the orientation of the beam trio in space.

The spatial distribution of these interference states can be predicted by mapping the conjugate signal clusters in the Fourier domain. Experimentally, observing these carrier waves serves as a diagnostic tool to verify the pulse train generation. If the beams arrive simultaneously, all beam pairs will interfere, resulting in a high number of cross-interference clusters. However, when a successful temporal separation is introduced, the cross-interference between the delayed and leading pulses ceases. This erases the unique cross-interference clusters and reduces the total number in the Fourier domain, confirming that a discrete pulse train has been formed and preparing the data for image reconstruction.

3.2 Experimental Procedures and Laboratory Execution

This section outlines how the system was operationally utilized in the laboratory to execute both static and dynamic measurements.

3.2.1 Static Characterization of Pulse Train Scalability

To characterize the FRAME system statically, air was used as the only medium. The purpose was to verify system stability and observe the resulting reference patterns and how they change depending on beam selection. No static characterization was performed for the Schlieren method, as the technique requires an active gradient to produce a signal.

3.2.2 2D Schlieren Imaging of Thermal Fluctuations

When testing the system with a flame, a CW laser was used instead of the pulsed laser. This served as a proof-of-concept for the 2D Schlieren method in a slow-moving environment before applying it to ultrafast phenomena like filaments. The goal was to demonstrate how the three-beam interference pattern can be utilized for 2D Schlieren measurements. The camera's shutter speed was set to be sufficiently short relative to the dynamic timescale of the flame, which effectively freezes the thermal fluctuations from the flame in the image. A flame is a well-understood phenomenon where temperature changes (and thus refractive index changes) are somewhat predictable, allowing for the verification of the method's accuracy.

The object (the Bunsen burner) was placed approximately 1.5 cm behind the focal plane. The use of a CW laser for the flame experiment simplified the timing, as the exposure did not need to be synchronized with a specific pulse train.

3.3 Data Acquisition and Image Reconstruction

Digital image processing is used to transform the raw camera images into either sequential movie frames or 2D gradient maps. This section describes how the image data was collected using synchronized triggers and how the MATLAB-based software operates in the Fourier domain to reconstruct the final images.

3.3.1 Sensor Specifications and Timing

The camera is used in conjunction with a trigger synchronized to the arrival of the laser pulse. For the pulsed laser experiments, the camera's shutter speed was long compared to the duration of the pulse train, resulting in the integration of the signal.

3.3.2 Image Processing and MATLAB Workflow

Existing MATLAB-based software, primarily utilizing Fourier analysis, is used to reconstruct images from the raw data. First, the data is Fourier transformed. The user then identifies the information clusters in the Fourier domain corresponding to the frequencies encoded in the image. This specific region is filtered out, and an Inverse Fast Fourier Transform (IFFT) is performed to recreate the image without the encoded pattern. The resulting image has a resolution corresponding to the size of the digital filter, which is lower than the original raw data. This represents the core trade-off of the FRAME method: spatial information is sacrificed to gain temporal information. When using a pulse train, this process is repeated for each sub-image by selecting different regions in the Fourier domain. Each filter produces one frame, which are then sequenced to form a video.

For the Schlieren analysis, MATLAB is also used to calculate refractive index variations based on pattern deformation. Each frequency component in the Fourier plane corresponds to a fringe pattern with a specific orientation in the spatial domain. The software analyzes how these fringes are locally displaced, providing information about the refractive index gradient in the direction perpendicular to the fringes. Since the pattern is created by three interfering beams, the image contains information from three different carrier wave directions. Each direction acts as a sensor for light deflection in that specific orientation. Mathematically, each component provides a gradient vector. By vectorially summing the information from these three components, the software calculates the complete refractive index gradient ∇n in two dimensions. The result is an image where the grayscale corresponds to the magnitude of the gradient. Unlike conventional 1D Schlieren, this method accounts for x and y gradient components simultaneously, transforming the patterned raw data into a composite shadowgraph showing the full 2D variation of the refractive index.

During the subsequent image reconstruction workflow in MATLAB, a digital spatial mask was applied to the captured raw data. This mask isolates only the region of interest containing the active reference pattern, as this patterned zone carries the modulated Schlieren phase information. To prevent edge artifacts and spectral leakage during the Fast Fourier Transform (FFT) processing, the boundaries of the digital mask were designed with a smooth, tapering gradient. This soft transition dampens high-frequency edge noise and averages out boundary discontinuities, ensuring a clean separation of the spatial frequency carrier waves and an accurate reconstruction of the 2D refractive index gradient.

4 Results

This chapter presents the experimental and theoretical validation of the simplified, common-path FRAME architecture. The evaluation is structured around three core performance metrics crucial for achieving single-shot ultrafast videography of stochastic phenomena. First, the structural simplification and its direct impact on material dispersion are quantified by comparing the glass path length against traditional systems. Second, the spatial frequency engineering and multi-beam interference principles are evaluated to demonstrate the system's framing capability and scalability. Finally, the capacity to extract comprehensive two-dimensional refractive index data from a single exposure is experimentally verified using a laboratory flame, demonstrating the architecture's readiness for capturing transparent, highly dynamic phenomena.

4.1 Optical Complexity and Dispersion Analysis

To benchmark the new architecture, in terms of dispersion and system complexity, a traditional FRAME configuration capable of generating a four-pulse train was analyzed (Figure 1). This conventional setup relies on six beam splitters, four diffractive optical elements (DOEs), and two lenses within the core FRAME imaging path. However, because the pulse splitting occurs along branched paths, an individual pulse within the train does not travel through every component on the table. To establish a fair baseline comparison for material dispersion, the traditional layout was scaled down to a two-pulse equivalent. For a two-pulse sequence, a single pulse physically passes through two beam splitters, one DOE, and two lenses. The resulting component count and effective material path lengths for both configurations, assuming a standard thickness of 5 mm per transmissive element, are summarized for direct comparison (Table1).

Parameter	**Traditional setup**	**New setup**
Lenses (5 mm)	2 pcs	1 pc
DOE (5 mm)	1 pcs	1 pc
Beam splitters (5 mm)	2 pcs	1 pc
Glass plates (1 mm)	0 pcs	1 pc
Total glass thickness	25 mm	11 mm

Table 1: Comparison between parameters of the traditional FRAME-setup, found in Figure 1 [13], (adapted for 2 pulses) and the new architecture used in this study.

Assuming an initial transform-limited pulse duration of 28 fs at a central wavelength of 840 nm, the temporal broadening due to group velocity dispersion (GVD) in fused silica was modeled using equation (7). Even when accounting for the branched path where a single pulse bypasses several components, the traditional system still accumulates an effective thickness of 25 mm, broadening the pulse significantly to 86.35 fs. In comparison, the compressed 11 mm glass path of the new architecture limits the total transmitted pulse duration to 45.56 fs. This quantitative reduction in pulse stretching shows that minimizing the physical path length preserves a shorter effective shutter speed.

In the traditional setup, adding more pulses quickly multiplies the total number of components. To evaluate the impact on dispersion, scaling relationships were derived in this work to describe how the maximum accumulated glass thickness depends on the desired number of pulses, n. Due to the branched nature of the traditional delay line, the effective material thickness experienced by a single pulse scales logarithmically. Assuming a standard thickness of 5 mm per transmissive optical element, the derived relationship for the traditional architecture dictates a total glass path of $15 + 10\log_2(n)$ mm for $n \geq 2$. In contrast, the maximum glass thickness in the new architecture scales strictly linearly, derived as

$10 + (n - 1)$ mm for $n \geq 1$, as extending the sequence length only requires inserting an additional 1 mm glass delay plate per added pulse. A consequence of this approach, however, is that individual pulses experience asymmetric dispersion; the delayed pulses accumulate more material path length than the leading pulse. This introduces a slight variation in pulse broadening across the pulse train, a limitation not present in the fully symmetric traditional configurations. Nevertheless, reducing the overall material path length to nearly half of the traditional baseline successfully minimizes the cumulative group velocity dispersion while establishing a highly simplified optical framework.

4.2 System Scalability and Sub-image Evaluation

Out of the 64 diffracted beams generated by the DOE, a subset of three beams is isolated using a custom spatial mask positioned in the focal plane of the lens (Figure 9a, Figure 6). Recombination of these three beams in the image plane produces a distinct, high-frequency spatial reference pattern recorded by the camera sensor (Figure 9b). Upon performing a 2D Fast Fourier Transform (FFT) on this raw image, each unique pair of interfering beams manifests as a distinct pair of conjugate signal clusters in the spatial frequency domain (Figure 9c). These cluster pairs are symmetrically arranged around the Fourier origin. The spatial separation of the beams in the physical Fourier plane directly dictates the radial distance of the clusters from the origin, while the geometric orientation of the beam pairs defines the angular position of the clusters in the frequency spectrum (Figure 9a, Figure 9c). Consequently, the maximum beam separation yields the outermost high-frequency clusters. Furthermore, the geometric angles between the beams in the physical optical domain correspond directly to the angular positions of the clusters in the image Fourier domain.

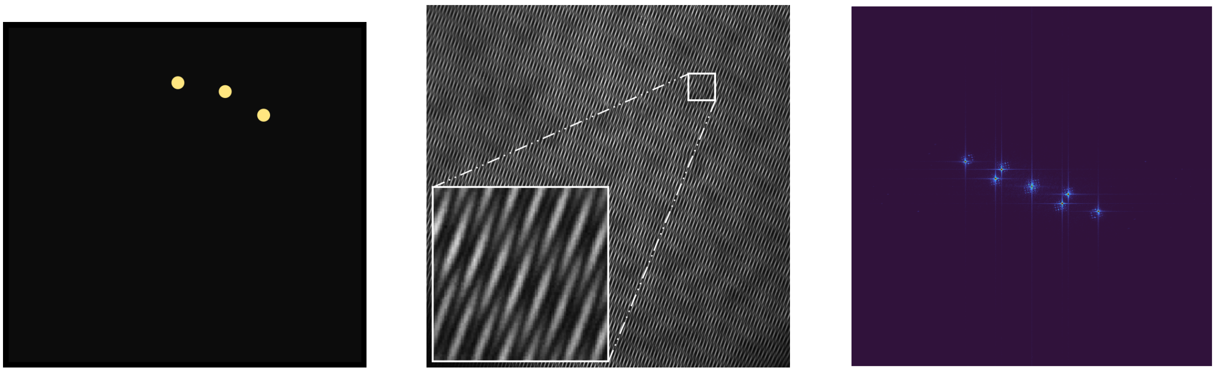

(a) Physical beam layout in the focal plane.

(b) The interference fringes recorded on the sensor.

(c) Image Fourier domain showing the signal spots.

Figure 9: Characterization of a single three-beam interference group, showing how the physical beam orientation dictates the spots in the Fourier domain.

An alternative triad of beams can be selected by rotating the spatial mask orientation within the optical Fourier plane (Figure 10a). While maintaining identical relative distances and internal angles as the first subset, this secondary triad is spatially rotated as a collective unit. This geometric shift reproduces the same underlying interference structure in the image plane, albeit with a corresponding spatial rotation on the sensor (Figure 10b). This physical rotation is directly reflected in the Fourier domain (Figure 10c), where the signal clusters rotate by the same angle. During these characterization measurements, the optical alignment remained highly stable, showing no measurable drift or need for realignment.

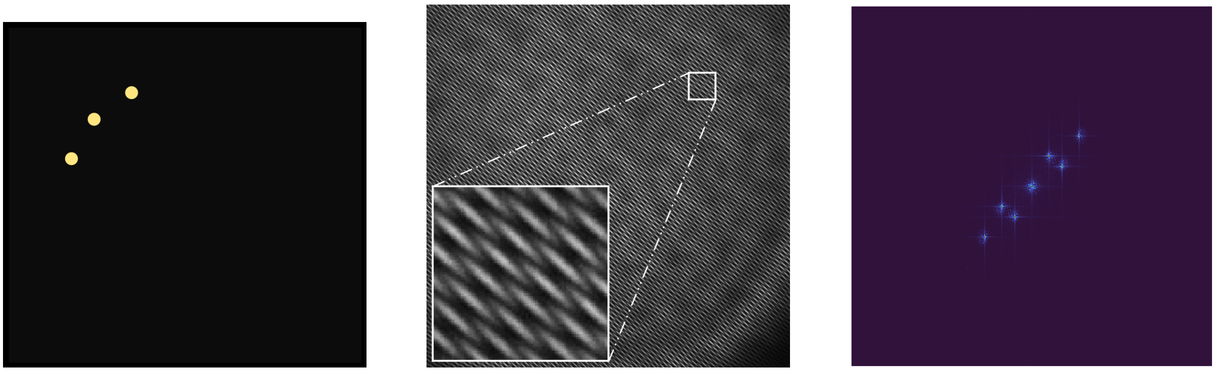

(a) Rotated beam layout after turning the spatial mask.

(b) The resulting rotated fringe pattern on the sensor.

(c) Image Fourier domain showing the corresponding rotation of the signal spots.

Figure 10: System response when rotating the spatial selection mask, demonstrating the predictable geometric mapping of the setup.

When all six beams are allowed to pass simultaneously without any time delay, a complex interference pattern arises (Figure 11b). Since each unique pair of beams generates its own carrier-wave cluster pair in the Fourier domain, six spatially co-located beams result in $\binom{6}{2} = 15$ cluster pairs (Figure 11c).

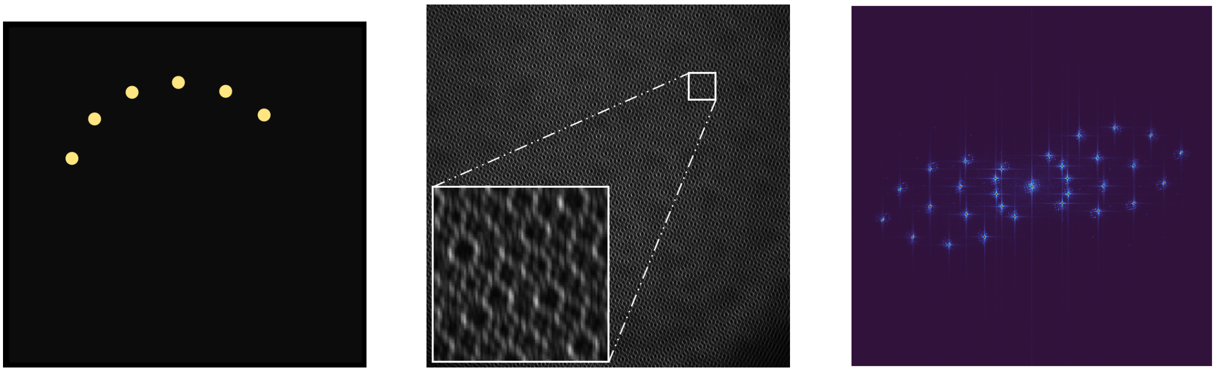

(a) Physical layout with all six beams unhindered.

(b) Complex grid-like interference pattern formed on the sensor.

(c) Image Fourier domain showing all 15 overlapping signal pairs before any time delay is introduced.

Figure 11: Interference structure generated by six overlapping beams without any temporal separation.

When a 1 mm thick glass plate is introduced into three of the beams (Figure 12a), the beams are divided into two temporally separated groups of three. This changes the Fourier domain significantly, reducing the number of visible cluster pairs from 15 to 6 (Figure 12c). The three delayed beams arrive at the image plane ~ 1.7 ps after the leading beams. Because of this temporal separation, beams from different groups no longer interfere with each other. While the internal interference within each three-beam group remains, producing $3 + 3 = 6$ cluster pairs, the 9 cross-interference cluster pairs between the two groups disappear. This experimentally confirms the creation of a temporally separated pulse train.

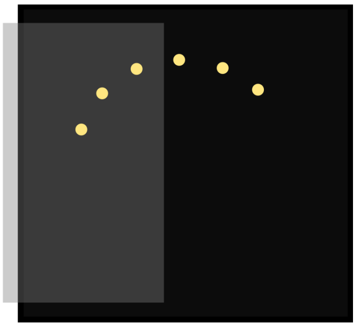

(a) Beam layout where three paths are delayed by a 1 mm glass plate.

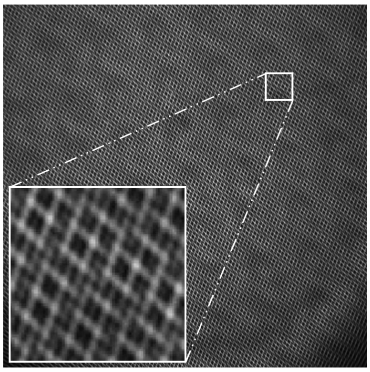

(b) Recorded fringe pattern on the sensor.

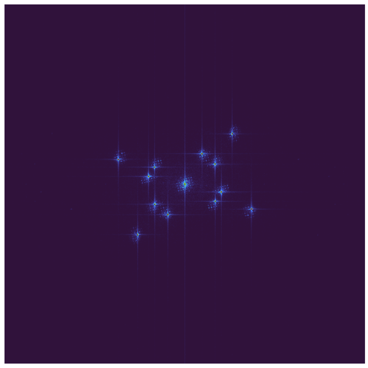

(c) Image Fourier domain where cross-talk spots disappear, leaving only 6 active pairs due to the time delay.

Figure 12: Experimental validation of a two-pulse train using six beams divided in time by a 1 mm glass plate.

By passing half of the selected beams through the 1 mm glass plate, the sub-pulses are split into two distinct arrival times at the image plane (Figure 12a). This introduces a calculated inter-frame delay of $\sim$ 1.7 ps according to equation (2). Demodulation and cross-talk-free image reconstruction of each temporal state are achieved by applying numerical bandpass filters to the respective non-overlapping cluster pairs in the Fourier domain (Figure 13a). Inverse Fourier transforming these isolated regions yields individual, unmodulated frames corresponding to the separate exposure times (Figure 13b, Figure 13c), which collectively form a two-frame video sequence. During this reconstruction, a faint residual background pattern can remain visible in the frames, which originates from the static diffraction structure of the DOE itself. However, because this structural pattern is constant over time, it can be entirely eliminated during data post-processing by subtracting a static background reference image.

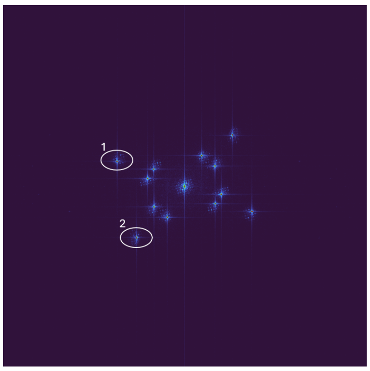

(a) Fourier spectrum with digital bandpass filters applied to isolate the pulses.

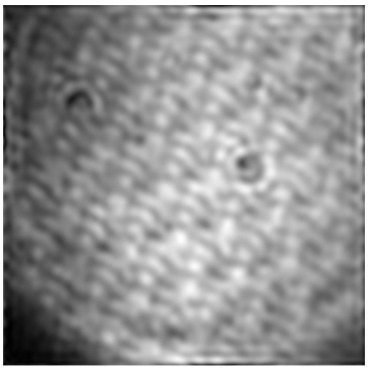

(b) Reconstructed image from the first pulse (no delay).

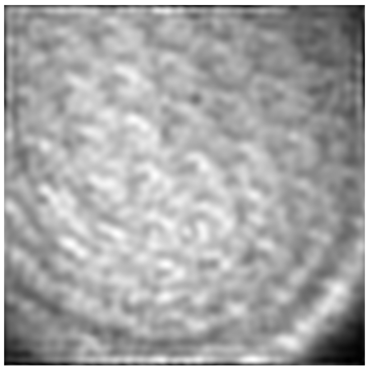

(c) Reconstructed image from the second pulse (1.7 ps delay).

Figure 13: Separated video frames extracted from the two-pulse train by filtering the independent Fourier spots.

Following the same operational principle, the sequence length was extended to a three-pulse train by deploying two stacked glass delay plates (Figure 14a, Figure 14b). In this configuration, two beams propagate unhindered through air, two pass through a single glass plate, and the final pair traverses both plates sequentially. The resulting multi-exposure frequency spectrum displays three independent pairs of active clusters without cross-talk interference (Figure 14c). Performing the spatial-frequency filtering routine on a single cluster representative of each discrete time step allows for the successful extraction of three independent, chronological frames, yielding a three-frame video sequence with a constant frame-to-frame interval of 1.7 ps (Figure 14d, 14e, 14f). The systematic transition from a two-frame to a three-frame sequence demonstrates the straightforward scalability of this single-shot ultrafast videography architecture. The ultimate boundaries for the maximum sequence length are dictated not only by the available geometric space for non-overlapping signal clusters in the Fourier domain but also by the cumulative material dispersion introduced as more delay plates are added to extend the sequence length. Each additional glass plate increases the medium thickness, causing the pulses to stretch more and more according to equation (7). If a pulse stretches too much and its duration approaches the 1.7 ps delay interval, it will start to overlap in time with the next pulse. This temporal overlap creates cross-talk between the frames, meaning that events from different time steps mix. Consequently, this pulse stretching sets a hard physical limit on how many frames can be added before the temporal resolution is lost.

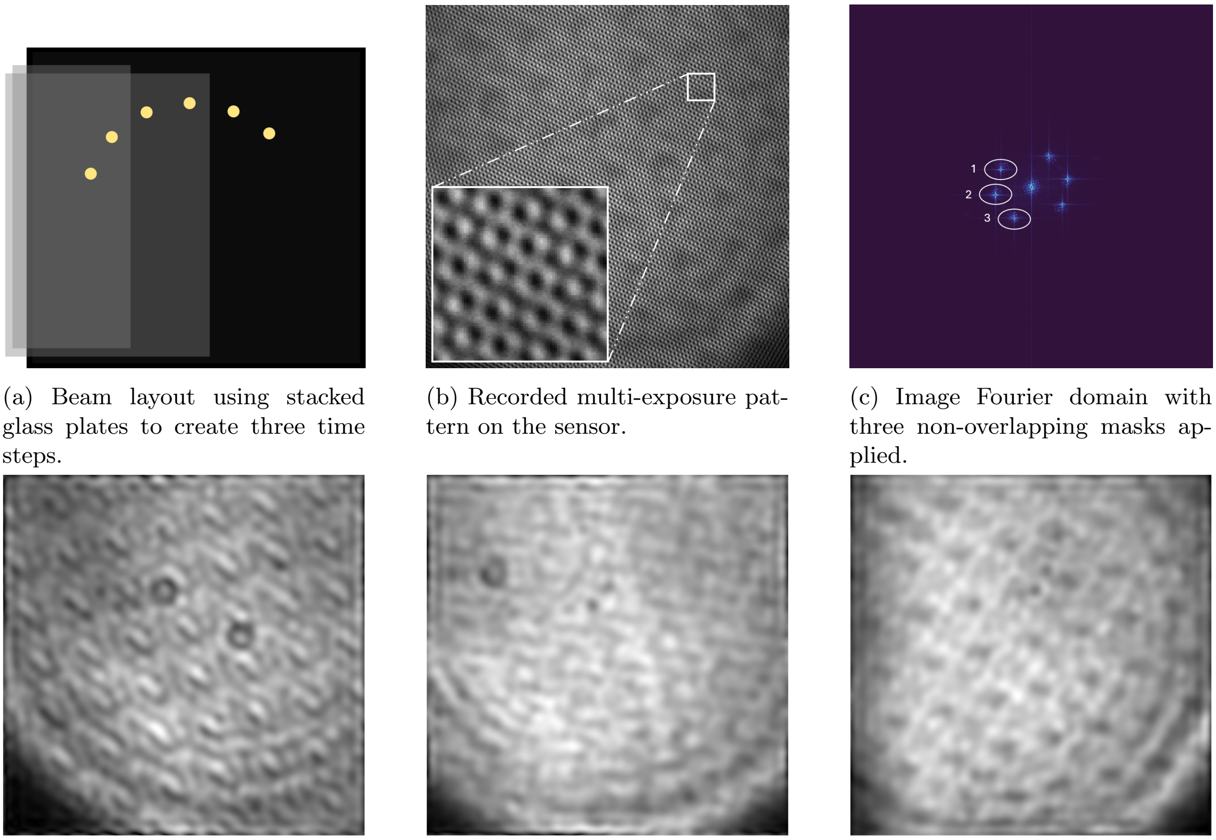

(a) Beam layout using stacked glass plates to create three time steps.

(b) Recorded multi-exposure pattern on the sensor.

(c) Image Fourier domain with three non-overlapping masks applied.

(d) Reconstructed image from frame 1 (t = 0 ps).

(e) Reconstructed image from frame 2 (t = 1.7 ps).

(f) Reconstructed image from frame 3 (t = 3.4 ps).

Figure 14: Reconstructed three-frame video sequence separated by a constant 1.7 ps interval.

4.3 2D Schlieren Extraction and Verification

Previous single-shot Schlieren FRAME techniques are fundamentally restricted by their 1D sensitivity [13], meaning they can only map refractive index gradients that line up perpendicular to a single set of interference fringes. For highly dynamic or chaotic structures like laser filaments, which exhibit variations in all spatial directions simultaneously, a 1D measurement yields an incomplete physical picture. The objective of the following evaluation is to experimentally demonstrate that by utilizing multi-directional three-beam interference, full 2D Schlieren data can be multiplexed and recovered from a single camera exposure.

To experimentally validate this 2D Schlieren capability, the architecture was transitioned from the pulsed femtosecond laser source to a continuous-wave (CW) laser. Consequently, the system no longer records a temporal pulse train, but rather a single-frame exposure. To achieve this, a three-beam spatial aperture mask was deployed in the optical Fourier plane (Figure 15a). It is critical to note that while the resulting image Fourier domain (Figure 15c) displays three pairs of conjugate signal clusters, visually mimicking the spectrum of the three-pulse train shown in Figure 14c, the underlying physical mechanism is fundamentally different. In the previous three-pulse experiment, the three spot pairs corresponded to three separate, temporally isolated pairs of beams forming consecutive frames over time. Here, the system utilizes a single triad of three beams allowed to pass simultaneously, where the three distinct spot pairs arise from the mutual cross-interference combinations ($\binom{3}{2} = 3$) of these co-propagating beams. This creates a complex grid-like spatial carrier pattern on the sensor within a single, non-temporal exposure (Figure 15b).

A dedicated phase-demodulation and Schlieren reconstruction algorithm was applied independently to each of the three frequency cluster pairs. This processing workflow extracts three separate orientation-specific Schlieren images, mapping the refractive index variations along each specific beam direction (Figure 16). For consistency, the color bars across all sub-frames share an identical scale.

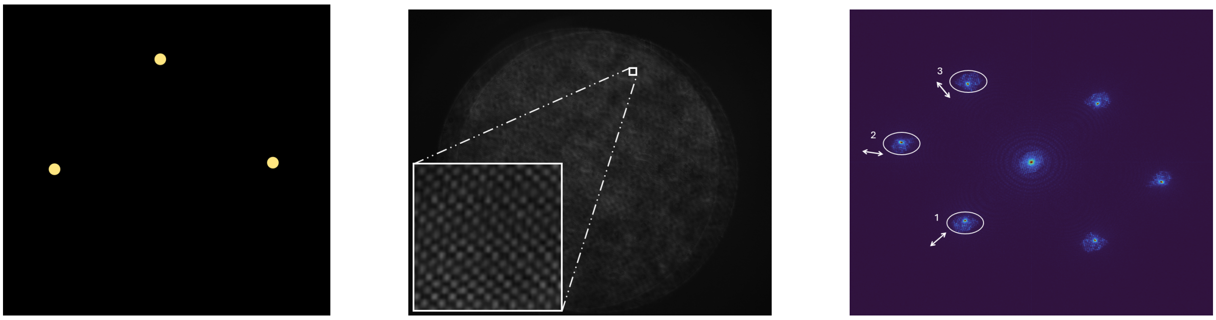

(a) Physical beam layout for Schlieren measurements.

(b) View of the reference pattern recorded before flame exposure.

(c) Image Fourier domain showing the three isolated pairs of signal spots used for the reconstruction. Carrier direction is indicated by the arrows.

Figure 15: Background reference calibration data used to establish the undisturbed phase baseline for 2D Schlieren imaging.

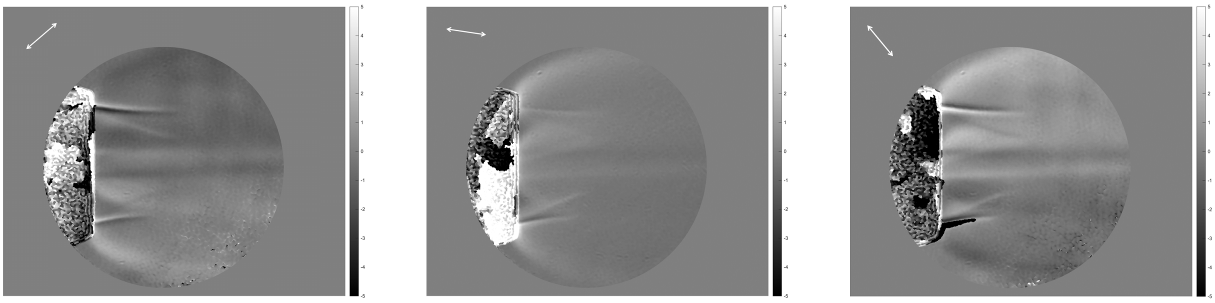

(a) Schlieren reconstruction along the first carrier direction.

(b) Schlieren reconstruction along the second carrier direction (blind to vertical gradients).

(c) Schlieren reconstruction along the third carrier direction.

Figure 16: Direction-specific Schlieren data extracted from each independent spot pair, illustrating how a single carrier direction (illustrated by the arrows) fails to capture the full shape of the flame.

The Schlieren reconstruction from each respective cluster pair (Figure 16) visualizes refractive index gradients that are strictly perpendicular to the carrier-wave fringes. This directional sensitivity is clearly visible when comparing the sub-frames. For instance, the center image (Figure 16b) appears mostly blind to the vertical heat gradients along the sides of the flame because the refractive index variations there occur horizontally, completely misaligned with that specific carrier projection vector.

This highlights a critical vulnerability in earlier single-shot methods, which were restricted to a single spatial carrier. In those setups, capturing a high-contrast image was largely a matter of luck. If the physical gradient happened to align parallel to the fringes, like in the center frame, virtually no information was recorded.

By instead combining these three different directional vectors, the system eliminates this reliance on luck and successfully maps the complete two-dimensional refractive index gradient ∇n (Figure 17a). When compared to a photographic reference state of the flame (Figure 17b), it is evident that the multidirectional approach successfully captures both the vertical thermal gradients along the sides of the flame and the horizontal variations in a single exposure. This tight agreement with the physical reference confirms that deploying a stable, multi-directional carrier pattern via three-beam interference provides a reliable method for capturing comprehensive, multi-directional refractive index variations instantaneously within a single camera exposure.

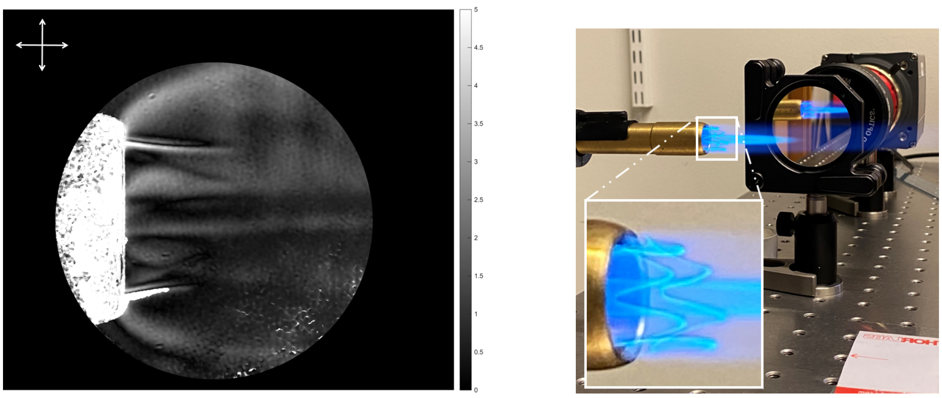

(a) The composite 2D Schlieren image representing the magnitude of refractive index gradient $|\nabla n|$. The bright white region to the left is the burner nozzle.

(b) A photographic reference picture of the physical Bunsen burner flame used during the validation measurements.

Figure 17: Final 2D Schlieren reconstruction results.

5 Discussion

This section evaluates the experimental findings of the compact FRAME architecture in relation to traditional configurations. By achieving a simplified common-path design, this work reconciles the trade-offs between sequence scalability, material dispersion, and directional refractive index gradient extraction. The following analysis evaluates the system's performance, assesses the reconstructed 2D Schlieren data, and outlines the practical limitations and future optimizations needed to transition this framework into practical ultrafast diagnostics.

5.1 Performance of the Compact Architecture

The compact configuration realized in this study results in a significant reduction in the number of components utilized, which clearly satisfies the requirement of reducing temporal dispersion and, at the same time, simplifies the alignment of the experiment. The typical FRAME setup is known to have a very complicated alignment that must be done every day because of its long optical path. As observed during the experimental evaluation, this newly realized compact setup has shown high stability, meaning that it remains aligned over extended periods of time without requiring realignment.

Furthermore, scaling the system to accommodate a longer pulse train relies solely on adding simple glass plates for temporal delays rather than incorporating additional bulky beam splitters and DOEs [15]. While past architectures required a large geometric footprint to generate spatial carrier patterns, the design presented here bypasses these requirements entirely. At its core, the pulse train can be generated using nothing more than a single DOE, a lens, and a glass plate. Because both the two-frame and three-frame variations of the pulse train (Figure 12 and 14) could be aligned by hand, the setup offers low operational complexity while maintaining high spatial reconstruction quality and system robustness.

A fundamental advantage of this FRAME architecture is that the pulse train generation and modulation are completely independent of the target object. Consequently, the system can image highly stochastic or entirely unknown ultrafast phenomena, such as turbulent flames or laser filaments.

Moreover, FRAME offers the unique capability to optically manipulate the pulses after the object plane without degrading the encoded temporal information. While minimizing glass thickness before the object plane is critical to mitigate group velocity dispersion (GVD), which temporally broadens the pulses and increases the effective exposure time, leading to motion blur, this constraint relaxes once the object has been exposed. In the object plane, the ultrafast temporal snapshot of the scene is instantaneously locked into the spatial carrier fringes. Any subsequent dispersion or temporal stretching experienced by the pulse packet during its remaining path to the sensor does not retroactively blur the captured event. This post-object independence opens up possibilities for downstream optical manipulation, such as filtering out only the wavelength of the imaging beam, thus blocking thermal radiation from a laser filament.

When generating the pulse train, the thickness of the glass plate directly dictates the time delay between two pulses according to equation (2). The 1 mm fused silica plate used in this work introduces a temporal delay of ~ 1.7 ps. When the pulse with the initial transform-limited pulse width of 28 fs travels through the plate, a frame rate of ~ 0.6 THz is achieved. To increase the frame rate, thinner glass plates can be deployed to reduce the temporal delay between pulses. To ensure successful image separation without temporal cross-talk, the pulses must be separated by at least $1.19 \cdot FWHM$ (~ 33 fs) [15]. According to equation (2), this defines a physical lower limit for the glass thickness at ~ 20 μm, giving a theoretical maximum frame rate of ~ 30 THz for a 28 fs pulse width. Naturally, the upper limit of the frame rate can be extended even further if shorter initial pulse durations are used. As higher frame rate makes it necessary to have thinner glass elements, the total material dispersion drops accordingly. A higher frame rate not only increases the temporal resolution, allowing rapid transient states to be resolved more clearly in the final video sequence, but also minimizes motion blur, thereby enhancing the overall image quality.

To comprehensively capture ultrafast events, both a high frame rate and an extended sequence length (number of frames) are required. Extending the sequence length requires scaling up the number of sub-pulses within the train, which is achieved by allowing the spatial mask to transmit more diffracted beams from the DOE. The absolute upper boundary for the sequence length is governed by the DOE, which in this setup divides the incoming beam into 64 separate profiles. Since a minimum of three beams is required per pulse to encode the 2D spatial carrier pattern, this specific DOE theoretically supports a maximum sequence length of $\frac{64}{3} \approx 21$ frames. To scale the sequence length beyond this limit, a custom DOE generating a larger array of diffracted beams could be integrated.

The second factor governing scalability is the accumulation of glass plates used for temporal delaying. The pulse subjected to the longest delay traverses the largest volume of glass and consequently experiences the most severe GVD. A hard physical limit is reached when the GVD broadens the pulse duration to a point where it exceeds the inter-frame delay step itself, a threshold calculated to occur at a total material thickness of approximately 400 mm of fused silica. Beyond this point, adjacent pulses will temporally overlap, causing them to co-expose the same temporal window and introduce severe motion blur. However, for the 64-beam DOE and the 1 mm glass plates used in this architecture, the geometric limitations of cluster packing in the Fourier domain restrict the sequence length long before material dispersion becomes a limiting factor.

5.2 Information Extraction and Schlieren Reconstruction Performance

The spatial carrier pattern generated via three-beam interference successfully addresses the requirement for extracting multi-directional refractive index gradients in a single exposure. This pattern proved highly straightforward to generate experimentally and remained exceptionally stable over time.

Previously, FRAME-based Schlieren setups achieved 2D gradient extraction for relatively slow phenomena, such as stable combustion, by recording two separate exposures in rapid succession using traditional two-beam interference oriented along different axes [13]. On those longer timescales, the flame structure remains stationary between frames, allowing for a successful 2D reconstruction of the refractive index gradient. However, this multi-exposure approach fails when capturing highly transient ultrafast events such as laser filaments, as the structure undergoes significant changes between successive frames. For such phenomena, all directional information must be captured instantaneously. Consequently, ultrafast Schlieren diagnostics have traditionally been restricted to 1D refractive index gradient extraction.

The compact architecture presented here overcomes this limitation by generating a three-beam spatial carrier pattern capable of capturing the complete 2D refractive index gradient within a single exposure (Figure 17a). Because this exact same multi-directional carrier pattern can be seamlessly multiplexed into a temporal pulse train (Figure 12, Figure 13), this architecture establishes a clear pathway for future studies to film the dynamic evolution of laser filaments with full 2D Schlieren capabilities.

However, certain regions within the reconstructed Schlieren images (Figure 16, Figure 17a) exhibit non-continuous boundaries and spatial phase "jumps" rather than smooth intensity gradients. These artifacts stem from localized failures in the digital phase-unwrapping algorithm. In regions where the flame introduces exceptionally steep refractive index gradients, or local intensity variations, the software fails to correctly track the phase continuity between adjacent pixels, resulting in sharp, nonphysical boundary discontinuities.

5.3 Practical Implications and Experimental Challenges

Despite the successful validation of the system, several experimental challenges were encountered during its implementation. A primary hardware constraint was that the available DOE was originally optimized for a different design wavelength, rather than the 840 nm central wavelength of the laser pulse used in this study. This mismatch resulted in an inefficient diffraction balance, generating an intense, undiffracted beam at the center of the pattern called the zeroth diffraction order. It also causes the higher diffraction orders to become severely unbalanced in intensity. Because this central spot carried a disproportionately high intensity, it threatened to saturate the dynamic range of the camera sensor. To protect the sensor and preserve image contrast, the zeroth order had to be physically blocked in the Fourier plane using a localized beam stop, which required precise manual positioning.

A second challenge relates to the physical dimensions and alignment of the prototype. Throughout this work, all optical masks, glass delay plates, and structural spacings were aligned and positioned manually. This manual approach limited how closely the components could be packed in the Fourier domain.

To transition this architecture from a laboratory bench top prototype to a highly optimized field-deployable diagnostic tool, these manual constraints can be removed. By utilizing automated manufacturing techniques, such as mounting high-precision, 3D-printed spatial masks and pre-aligned glass delay plates directly onto a dedicated short-focal-length lens assembly, the entire system could be drastically miniaturized. Such an integrated, pre-aligned design would eliminate manual alignment errors entirely, transforming this advanced ultrafast imaging system into a highly compact, robust, and "plug-and-play" instrument suitable for industrial and multi-user research environments.

5.4 Future Work

To transition the current compact FRAME architecture from a successful proof-of-concept prototype to a high-performance diagnostic tool, several key advancements in both hardware and software should be pursued in future work.

5.4.1 Optimization of Diffractive Optics

The integration of a custom DOE precisely etched for the central laser wavelength of 840 nm represents an immediate hardware improvement. This would eliminate the high-intensity zeroth diffraction order, thereby removing the need for a manual beam stop and maximizing the dynamic range available on the camera sensor. Furthermore, matching the laser wavelength would suppress the unwanted scattering of light into unintended diffraction orders, thereby reducing the residual background patterns that persisted in the final reconstructed images. Additionally, a custom DOE could be designed to distribute the pulse energy more uniformly across a larger array of beams, allowing for longer video sequences.

5.4.2 System Miniaturization and Automated Manufacturing

Future iterations should leverage fabrication and additive manufacturing to commercialize the setup. Designing a 3D-printed aperture housing that pre-aligns the custom spatial masks and glass delay plates directly onto a short-focal-length imaging lens would eliminate all manual alignment errors. This would drastically compress the physical distance between the DOE and the sensor, creating a highly robust, "plug-and-play" optical module suitable for challenging industrial or multi-user laboratory settings.

5.4.3 Enhanced Phase-Unwrapping Algorithms

To address the localized phase "jumps" and continuous boundary artifacts observed in the 2D Schlieren reconstructions, more sophisticated digital processing routines are required. Implementing more robust phase-unwrapping algorithms could significantly improve the software's resilience to steep refractive index gradients, yielding artifact-free 2D gradient maps even in highly turbulent environments.

5.4.4 Application to Ultrafast Stochastic Phenomena

With the 2D Schlieren capability and temporal multiplexing successfully verified using a stable flame, the next logical step is to deploy the system to capture true sub-picosecond, non-repetitive events. Future experiments should focus on imaging the dynamic evolution of laser filaments, plasma formation, or localized aerodynamic shockwaves. Capturing these phenomena will fully exploit the system's ultrafast frame rates ($\sim$ 0.6 THz to $\sim$ 30 THz) and its unique capacity for single-exposure 2D extraction.

6 Conclusion

This study has successfully developed and validated a compact and robust FRAME-architecture with a minimized number of optical components, which directly meets the system design goals. By replacing the traditional, spacious beam splitters and DOEs with a common-path configuration based on a single DOE, a lens, and simple glass plates, the system alignment has been significantly simplified, while the mechanical stability has been improved. The total path length through glass has been reduced to nearly one-third compared to the prior FRAME system. It was calculated that a 1 mm glass plate generates a 1.7 ps temporal delay for a 28 fs laser pulse, resulting in a frame rate of 0.6 THz. The architecture also shows a high theoretical limit for the time resolution by using thinner glass plates (down to $\sim$20 μm), giving a frame rate up to 30 THz, before the pulses overlap in time.

Regarding the scalability of the system, the study shows that the architecture allows for an uncomplicated increase in the number of frames in the sequence by adding more delay plates to the beam path. The maximum sequence length is currently limited by the number of beams generated by the DOE and by the geometric space for signal reconstruction in the Fourier domain, rather than by pulse width extension caused by material dispersion. The critical dispersion limit where adjacent pulses merge is estimated to occur only at a total glass thickness of approximately 400 mm of fused silica, which means that the current optical design has significant scope for further scaling up the number of frames.

Finally, the research has successfully been able to implement and evaluated a method for generating stable reference patterns through three-beam interference. This made it possible to extract complete, two-dimensional (2D) refractive index gradients in a single exposure, which was validated through Schlieren imaging of a Bunsen burner. By eliminating the need for multiple exposures to obtain 2D information, this architecture overcomes the prior limitations for ultrafast Schlieren diagnostics. In conclusion, the developed system provides a reliable and scalable architecture enabling future studies of stochastic phenomena on the sub-picosecond timescale, such as the dynamic evolution of laser filaments.

References

[1] A. Couairon and A. Mysyrowicz. “Femtosecond filamentation in transparent media”. In: *Physics Reports* 441.2 (2007), pp. 47–189. ISSN: 0370-1573. DOI: https://doi.org/10.1016/j.physrep.2006.12.005. URL: https://www.sciencedirect.com/science/article/pii/S037015730700021X.

[2] Huai Liang Xu and See Leang Chin. “Femtosecond Laser Filamentation for Atmospheric Sensing”. In: *Sensors* 11.1 (2011), pp. 32–53. ISSN: 1424-8220. DOI: https://doi.org/10.3390/s110100032.

[3] Ludger Wöste, Steffen Frey, and Jean-Pierre Wolf. “LIDAR-Monitoring of the Air with Femtosecond Plasma Channels”. In: ed. by G. Rempe and M.O. Scully. Vol. 53. Advances In Atomic, Molecular, and Optical Physics. Academic Press, 2006, pp. 413–441. DOI: https://doi.org/10.1016/S1049-250X(06)53011-3.

[4] Jiayun Xue et al. “Air Waveguiding of Lasing Induced by Long-Distance Filament”. In: *Laser & Photonics Reviews* (2026). Jiayun Xue and Lu Sun contributed equally to this work. DOI: 10.1002/lpor.71025.

[5] Pengfei Qi et al. “Sensing with Femtosecond Laser Filamentation”. In: *Sensors* 22.18 (2022). ISSN: 1424-8220. DOI: https://doi.org/10.3390/s22187076.

[6] Manabu Suzuki et al. “Over 100 Million Frames per Second 368 Frames Global Shutter Burst CMOS Image Sensor with Pixel-wise Trench Capacitor Memory Array”. In: *Sensors* 20.4 (2020). ISSN: 1424-8220. DOI: 10.3390/s20041086.

[7] Takeharu Goji Etoh et al. “The Theoretical Highest Frame Rate of Silicon Image Sensors”. In: *Sensors* 17.3 (2017). ISSN: 1424-8220. DOI: 10.3390/s17030483.

[8] Ahmed H. Zewail. “Femtochemistry: Atomic-Scale Dynamics of the Chemical Bond”. In: *The Journal of Physical Chemistry A* 104.24 (2000), pp. 5660–5694. DOI: 10.1021/jp001460h. eprint: https://doi.org/10.1021/jp001460h. URL: https://doi.org/10.1021/jp001460h.

[9] Royal Swedish Academy of Sciences. *Scientific Background on the Nobel Price in Physics 2023: For experimental methods that generate attosecond pulses of light for the study of electron dynamics in matter.* Tech. rep. The Royal Swedish Academy of Sciences, Oct. 2023.

[10] Liang Gao et al. “Single-shot compressed ultrafast photography at one hundred billion frames per second”. In: *Nature* 516.7529 (2014), pp. 74–77. DOI: 10.1038/nature14005. URL: https://doi.org/10.1038/nature14005.

[11] Jingzhen Li et al. “Advances in Atomic Time Scale Imaging with a Fine Intrinsic Spatial Resolution”. In: *Ultrafast Science* 4 (2024), p. 0046. DOI: 10.34133/ultrafastscience.0046. URL: https://doi.org/10.34133/ultrafastscience.0046.

[12] Andreas Ehn et al. “FRAME: femtosecond videography for atomic and molecular dynamics”. In: *Light: Science & Applications* 6.9 (Sept. 2017), e17045. DOI: 10.1038/lsa.2017.45.

[13] Simon Ek et al. “High-speed videography of transparent media using illumination-based multiplexed schlieren”. In: *Scientific Reports* 12.1 (2022), p. 19018. DOI: 10.1038/s41598-022-23198-6.

[14] Bahaa E. A. Saleh and Malvin Carl Teich. *Fundamentals of Photonics*. 3rd. Wiley Series in Pure and Applied Optics. Hoboken, NJ, USA: Wiley, 2019. ISBN: 978-1119506874.

[15] Simon Ek. “Optical Multiplexing for Ultrafast Videography”. Lund Reports on Combustion Physics, LRCP-238. PhD thesis. Lund, Sweden: Division of Combustion Physics, Lund University, May 2024.